Origin of Performance Improvements in Lithium-Ion Cells after Fast Formation

Daniel Witt,[a, b, c] Lars Bläubaum,[a] Florian Baakes,[a] and Ulrike Krewer*[a]

The formation process of lithium-ion batteries commonly uses low current densities, which is time-consuming and costly. Experimental studies have already shown that slow formation may neither be necessary nor beneficial for cell lifetime and performance. This work combines an experimental formation variation with physicochemical cell and solid electrolyte interphase (SEI) modeling to reveal formation-induced changes within the cells. Formation at C/2 without full discharge compared to a standard C/10 formation at 20 °C notably improves the discharge and charge capacities at 2C by up to 41 % and 63 %, respectively, while reducing the formation time by over 80 %. Model-based cell diagnostics reveal that these performance gains are driven by improved transport in the anode electrolyte phase, which is affected by SEI formation, and by enhanced transport on the cathode side. Hence, the focus on the dense SEI layer is insufficient for a comprehensive understanding and, ultimately, optimization of cell formation. All formation procedures were also tested at temperatures of 35 °C and 50 °C. Despite often surpassing the 2C discharge capacity of the standard formation at 20 °C, these cells showed comparable or lower 2C charge capacities. This suggests a pivotal role of local temperature in the formation of large-format cells.

Introduction

Lithium-ion batteries have become an integral part of our everyday life, powering mobile applications ranging from consumer electronics to electric cars and even future airplanes.[1,2] Consistent improvements in cell lifetime, performance, and production costs have put lithium-ion battery technology in a unique position to enable the electrification of the transportation sector. Apart from long-term environmental and economic advantages, recent geopolitical uncertainties have also highlighted the benefit of a more self-sufficient energy supply based on renewable energies.

Impact of Cell Formation

Considering the expected massive increase of battery production capacity in the years to come,[3,4] any improvement of production processes and cell quality will have a huge impact on its overall resource efficiency. The total cost of a lithium-ion battery can be divided into roughly 75 % material costs and 25 % production costs.[5,6] To facilitate meaningful innovations in battery production, a thorough understanding of cost, time demand, and energy consumption of state-of-the-art production processes is crucial. The cell formation and the subsequent cell aging combined are currently the most cost-sensitive process steps toward the end of battery production, accounting for roughly 30 % of the production cost of lithium-ion batteries.[5,7,8] For comparison, electrode coating and drying contribute about 15 % to the total production cost, while enclosing and electrolyte filling constitute about 13 %.[7,8]

Regarding production throughput, the formation and aging processes are a clear bottleneck with process times up to multiple days for formation and multiple weeks for aging.[9] This also explains the large number of battery cyclers and the substantial floor space requirements of up to 25 % of the entire production facility, presenting a unique opportunity for meaningful optimizations.[9] In terms of energy consumption, cell formation is less critical due to the recycling of discharged energy, resulting in a share of about 1 % to 5 %.[8,10,11] Electrode drying and solvent recovery offer a much more significant potential for energy savings with a share of roughly 47 % and dry room operation with about 29 %.[8]

The time requirement of the cell formation process is related to the commonly applied low current densities, which are intended to create a well protective solid electrolyte interphase (SEI). This surface film formation is inevitable due to the large voltage window of lithium-ion batteries in contrast to the much smaller stability window of standard electrolyte systems.[12] Once established, the SEI suppresses ongoing side reactions, ensures a high coulombic efficiency, and results in a reliable and stable battery performance.[13,14] Without a sufficiently passivating SEI, side reactions would continue to

[a] D. Witt, L. Bläubaum, F. Baakes, U. Krewer
Institute for Applied Materials – Electrochemical Technologies, Karlsruhe Institute of Technology, Adenauerring 20b, 76131 Karlsruhe, Germany
E-mail: ulrike.krewer@kit.edu

[b] D. Witt
Institute of Energy and Process Systems Engineering, TU Braunschweig, Langer Kamp 19b, 38106 Braunschweig, Germany

[c] D. Witt
Battery LabFactory Braunschweig, TU Braunschweig, Langer Kamp 8, 38106 Braunschweig, Germany

Batteries & Supercaps

Research Article
doi.org/10.1002/batt.202400023

**Chemistry
Europe**

European Chemical
Societies Publishing

consume cyclable lithium and, as a side effect, ongoing SEI growth would deteriorate transport in an increasingly less porous electrode. Both aspects decrease the practical capacity and energy density of the cell. For this reason, a sound understanding of the impact of formation conditions like current density, voltage range, and temperature on performance-limiting and degradation-related cell properties is crucial for knowledge-based optimizations.

After formation, an aging procedure is applied with two main goals: i) facilitate the naturally occurring restructuring of the SEI after its initial formation[15,16] and ii) enable a classification of the final cells, commonly based on their self-discharge over multiple weeks.[5,17] To the best of the authors' knowledge, a dedicated study on the impact of this process on the fast charge/discharge and aging characteristic of a cell is not yet available. Thus, the actual optimization potential for meaningful time savings without a compromise in terms of cell quality remains unclear. However, different approaches have been patented to enable a substantially faster quality classification, e.g., by measuring a self-discharge current over hours rather than a self-discharge voltage over weeks[18] or by estimating self-discharge via calorimetry.[19]

Cell Formation Approaches

Due to their huge impact on cell lifetime and performance, commercially used cell formation procedures and electrolyte compositions are well-protected corporate secrets.[9] Schomburg et al. provide a comprehensive review on the cell formation process, highlighting the rarity of systematic variations of this cell quality-defining process step in scientific literature.[20]

In literature, various studies achieve improved cell characteristics with different formation procedures but, at first sight, surprisingly similar explanations. For example, An et al. proposed shallow formation cycling above 3.9 V, essentially avoiding full depth-of-discharge cycles and focusing on the high cell voltage regime, i.e., low anode potentials.[21] Müller et al. found a clear benefit for the constant-voltage charging step during formation, ensuring low anode potentials over an extended time.[22] Mao et al. investigated formation protocols with various C-rates.[23] They found that the best cell characteristics could be achieved neither with the fastest formation due to lithium plating nor the slowest procedure. Röder et al. investigated surface film formation at different C-rates by coupling a continuum pseudo-two-dimensional (P2D) model with a stochastic SEI growth model.[24] They found that medium C-rates offer a trade-off between the spatial heterogeneity of the SEI at higher C-rates and the prevailing stochastic effects on SEI composition and structure at lower C-rates. Drees et al. used an equivalent circuit model to minimize the formation time while maintaining similar aging characteristics compared to a slower formation.[25] For their optimization, they considered a lower limit for the anode potential of 10 mV vs. Li/Li$^+$ to prevent lithium plating. Overall, these studies mirror the general understanding within the battery community that a well-

protective, dense, and stable SEI is predominately formed at low anode potentials below 0.5 V or even 0.25 V vs. Li/Li$^+$.[15,26,27] Here, fast formation seems generally favorable as long as substantial lithium plating is prevented.

Apart from production economics, which is closely related to formation time, the final cell quality must be evaluated. The capacity retention and the impedance rise along aging are often used for benchmarking different formation procedures.[21–23,25,28] Some studies also report the rate performance of the cells, but do not see substantial differences in discharge capacity.[21,23] Although most applications demand a minimal recharge time to enable an almost uninterrupted mobile power supply, the fast charge capability is only rarely reported.

SEI Formation and Evolution

Forming a stable SEI is challenging as it is influenced by various aspects like formation conditions (current density profile, temperature, pressure), electrolyte composition, active material system, and surface modifications.[17,29] In general, the formation of the SEI on carbonaceous anode active material particles originates from the reductive decomposition of the electrolyte. Commonly observed SEI components after cell formation comprise inorganic species, like lithium fluoride (LiF) and lithium carbonate (Li$_2$CO$_3$), close to the particle surface and organic species, like lithium ethylene dicarbonate (LEDC), in a more porous secondary layer.[13] However, a study on reaction products with the common electrolyte component ethylene carbonate (EC) detected only LEDC and no lithium carbonate.[30] A complementary analysis of the SEI component LEDC revealed that its degradation leads to a more complex SEI composition and structure, including Li$_2$CO$_3$ and various organic salts.[31] Eventually, elevated formation currents could also affect the SEI composition and structure, e.g., due to concentration deprivation of low-concentration electrolyte additives at the particle surface. This could trigger a transition between different SEI growth reactions.

The initially formed SEI has various vulnerabilities and weak points. It is commonly agreed upon the occurrence of further SEI growth during cell aging.[32–34] This is attributed to slowly progressing side reactions,[35,36] mechanical degradation of the surface film with a subsequent rapid SEI reformation,[37] transition metal deposition in the SEI from the cathode,[38] and crossover of electrolyte oxidation products from the cathode side, which degrade first the conductive salt LiPF$_6$[39] and afterward the SEI.[40] This adds to the complexity of possible reasons for an evolution of the SEI composition and its effective properties along aging.

Elevated cell temperatures further strain the stability of the SEI and the electrolyte system. Parimalam et al. demonstrated that elevated temperatures of only 55°C already result in the decomposition of lithium carbonate and LiPF$_6$ into CO$_2$, LiF, and F$_2$PO$_2$Li.[41] They repeated the study with LEDC instead of lithium carbonate and observed an even higher reactivity. The reaction products also became much more diverse in this case, including

Batteries & Supercaps

Research Article
doi.org/10.1002/batt.202400023

Chemistry Europe
European Chemical
Societies Publishing

phosphates, fluorophosphates, and oligoethylene oxides. In the context of cell formation, such a thermal SEI decomposition could interfere with the formation of a robust SEI structure at elevated formation temperatures. This is not only important for the choice of an optimal formation temperature. It also suggests that large temperature gradients within a cell during formation may result in a location-dependent SEI composition and structure.

SEI Characterization

Experimental methods for the characterization of the SEI generally require a special cell preparation that may not be representative of commercial cells anymore. However, they can offer valuable understanding of SEI composition and structure.[42–44] Model-based approaches promise to extract hardly measurable parameters from simple measurements, often using either cycling data[33,36] or electrochemical impedance spectra.[34,45,46] In the former case, insights into SEI changes are commonly limited to the loss of cyclable lithium that is attributed to SEI growth. With EIS-based cell state estimation, changes in SEI-related process kinetics and double-layer capacitances become accessible. Here, equivalent circuit models (ECM) have proven themselves as a valuable tool for impedance analysis as they can be easily adjusted to represent various impedance spectra.[45,47] However, ambiguities may arise if an ECM is not backed by a physics-based analogy, complicating the interpretation of its parameters.[48]

As shown by our previous study, the analysis of a broad range of operational modes is crucial for a proper parameter estimation in a P2D model[49] including the SEI.[50] The estimated parameters within the physicochemical cell and SEI model are inherently more insightful as they are valid for discharge and impedance data. This ensures that processes and their impact on performance can be reliably identified, differentiating between charge transfer kinetics, SEI properties, and transport in the solid and electrolyte phase. In addition, model-based cell diagnostics allows to estimate parameters that are experimentally difficult to measure, such as the anode tortuosity after formation. Although symmetric EIS measurements with a non-intercalating electrolyte could provide an estimate of this parameter,[51] the extraction and preparation of the electrodes from full cells would likely remove at least part of the SEI. Furthermore, such measurements are destructive, i.e., monitoring the evolution of the parameters in the same cell during cycling is not possible.

To close the knowledge gap between industry and academia, systematic research on the intricate interplay between cell formation, cell performance, and performance-defining cell properties is needed. The goal of this work is a better understanding of the physical effects that formation procedures have on the cell and SEI state. Specifically, we perform an experimental formation study inspired by recommendations from literature. For deeper insights into the effect of formation temperature on cell performance, all formation procedures are investigated at 20 °C, 35 °C, and 50 °C. In contrast to other studies, we assess both the fast discharge and the fast charge capability to obtain a more comprehensive picture of the effect of cell formation. Focusing on the best-performing cell, we employ for the first time physicochemical cell and SEI modeling to identify and quantify formation-induced changes in electrode- and particle-level cell properties.

Experimental Section

Cell Setup

The cells in this work use graphite and NMC622 as the anode and cathode active materials, respectively. The electrodes were produced in the Battery LabFactory Braunschweig. They have an active material content of 93 % with a final electrode porosity of 37 % for the anode and 24 % for the cathode.[50] All experiments were performed with the commercial PAT-Cell three-electrode setup by EL-Cell GmbH. For this setup, the electrodes were punched to a diameter of 18 mm, weighed, and dried at 120 °C under high vacuum. The subsequent cell assembly was done in an argon-filled glovebox. A polypropylene fiber/polyethylene membrane separator by EL-Cell GmbH with an integrated lithium-metal reference electrode was used (ECC1-00-0210-V/X) to complete the three-electrode setup. The cells were filled with 100 µL electrolyte, i.e., 1 M LiPF$_6$ conducting salt in a 3:7 (v:v) solvent mixture of ethylene carbonate (EC) and ethyl methyl carbonate (EMC) with 2 wt% vinylene carbonate (VC).

Formation Process

A complete infiltration of the porous cell structure with electrolyte is crucial for a successful cell formation. Otherwise, SEI growth and current density distribution could be highly inhomogeneous throughout the cell, leading to unpredictable cell characteristics and potential cell failure.[52] For this reason, all formation variations are preceded by a 12 h rest time. Afterward, two formation cycles are applied. All variations of formation procedure and temperature are summarized in Table 1. The formation with a C-rate of C/10, named F@C/10, and a temperature of 20 °C is used as a reference. The faster formation procedure, F@C/2, and the literature-inspired formation with a lower cutoff voltage of 3.7 V in the first cycle, F@C/2$_{3.7V}$, are added to distinguish the impact of higher formation currents and the effect of low anode potentials over an extended time, respectively.[21] Besides 20 °C, elevated formation temperatures of 35 °C and 50 °C are used to study the effect of faster reaction kinetics and transport processes on SEI formation. The higher temperatures essentially emulate notable self-heating in large-format cells without active cooling. As discussed earlier, the

Table 1. Variations of the cell formation process regarding applied C-rate and temperature. In charge direction, a constant-voltage step with a cutoff C-rate of C/20 is added. The cutoff voltages for charge and discharge are 4.2 V and 2.9 V, respectively. The variation F@C/2$_{3.7V}$ without full depth of discharge uses a lower cutoff voltage of 3.7 V in the first formation cycle.

Formation procedure	F@C/10	F@C/2	F@C/2$_{3.7V}$
Temperature / °C	20, 35, 50	20, 35, 50	20, 35, 50
Charge rate in 1st cycle	C/10	C/2	C/2
Discharge rate in 1st cycle	C/10	C/2	C/2 ≥ 3.7 V
Charge rate in 2nd cycle	C/10	C/2	C/2
Discharge rate in 2nd cycle	C/10	C/2	C/2

Batteries & Supercaps

Research Article
doi.org/10.1002/batt.202400023

Chemistry Europe
European Chemical
Societies Publishing

omission of the constant-voltage charging step could provoke the formation of an insufficiently protective SEI.[22] For this reason, all formation variations include this step in charge direction.

Electrochemical Characterization

Cell formation and cycling were done with an automated MACCOR series 4000 test system. EIS measurements were conducted with a Gamry Interface 5000E potentiostat/galvanostat. All measurements were carried out in an ESPEC SU-641 temperature chamber at 20 °C or, for formation at elevated temperatures, at 35 °C and 50 °C. The C-rates for cell formation and the subsequent cell cycling are defined based on the theoretical capacity of the cathode, i.e., the weight of the individual electrodes. Two cells were assembled and tested for each formation variation.

After formation, a capacity test at a C-rate of C/10 is applied to determine the practical capacity of the cell, which is used to estimate the initial capacity loss and to approximate the initial SEI thickness.[50] Subsequently, a characterization procedure is applied, which comprises an EIS measurement and a C-rate test at various C-rates. Afterward, the cells undergo 50 charge-discharge cycles between 2.9 V and 4.2 V, followed by the same characterization procedure as before. This combination of cycling and characterization procedure is repeated for a total of 100 cycles and three detailed electrochemical characterizations (see Supporting Information, Table S1).

Computational Methods

Model Setup

The cell and SEI model in this work is adopted from our previous work.[50] It is based on the P2D battery model by Doyle et al.[53] with electrochemical double-layers at the active material particle surface as proposed by Legrand et al.[54] Herein, both the electrode and the active material particles are spatially discretized, which allows for a sufficiently accurate description of experimental data with moderate computational effort. Contact-resistance-related dynamics are considered at both current collectors.[50,55]

The SEI as a surface film has two interfaces: one with the underlying active material particle (sSEI), and one with the electrolyte phase (SEIe). Both interfaces feature an electrochemical double-layer with capacitances $C_{DL,sSEI}$ and $C_{DL,SEIe}$, respectively, as well as a limited number of surface sites Γ_{SEI} for occupation by lithium-ions. The path of a lithium-ion from the active material to the electrolyte phase comprises three process steps. It starts with the deintercalation from the active material, continues with the transport through the SEI via migration and diffusion, and ends with the desorption at the outer interface of the SEI. Here, we adopt a transference number of $t_{p,SEI} = 0.97$ from Single et al., which almost corresponds to a single ion conductor.[56] The governing model equations for the SEI model are summarized in the SI, Table S3. As the overall impact of cathode-side surface film formation is generally expected to be less pronounced, it is modeled SEI-free.[13] The general P2D model and further complementary equations are given in the SI, Table S4 and Table S5, respectively.

For the modeling of the SEI, we assume spherical anode active material particles. The SEI thickness d_{SEI} is directly linked to the specific surface area of the anode active material and the loss of lithium inventory. Similar to other simulation studies, we approximate the multi-component nature of the SEI with only one species.[34,36,57] Due to the evolution of the SEI during cycling toward

a more inorganic structure,[58] we consider pure lithium carbonate according to the following reaction:[12]

$$EC + 2Li^+ + 2e^- \rightarrow Li_2CO_3 + C_2H_4 \tag{1}$$
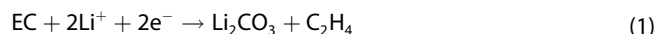
Notably, the SEI thickness also reduces the porosity of the anode, which deteriorates transport in the electrolyte phase. The lower density of the organic SEI component LEDC would intensify such transport limitations, given the same loss of lithium inventory.[59]

The initial capacity loss is estimated based on the charged capacity in the first formation cycle compared to the discharge capacity in the third cycle, i.e., the first cycle after cell formation. Similar to our previous work, the voltage at the end of discharge is used to separate a state-of-charge shift and SEI growth within the first charge cycle.[50]

Parameterization Strategy

For a meaningful model-based cell diagnosis, we employ a three-step parameterization strategy for the initial cell state estimation and the parameter update along aging.[50] This procedure takes advantage of different parameter sensitivities in discharge curves and EIS measurements, using a three-electrode setup.

Table 2 summarizes the parameters and experimental data that are considered in each parameterization step. First, the available lithium inventory after cell formation is extracted from C/10 discharge curves, comprising the SEI thickness d_{SEI} and the initial and maximum lithium concentrations in the anode ($c_{0,a}$, $c_{max,a}$) and cathode active materials ($c_{0,c}$, $c_{max,c}$). Here, the initial cell state estimation based on cycle 0 is unique as it can also use cell formation data. This enables a direct calculation of d_{SEI} based on the initial capacity loss. Higher C-rates of 1C and 2C provide insights into effective transport properties in the solid and electrolyte phase, comprising the tortuosity of anode τ_a and cathode τ_c, as well as the cathode solid diffusion coefficient $D_{s,c}$. The anode solid diffusion coefficient is adopted from our previous work as it did not show notable sensitivity.[50] Finally, kinetic parameters and process dynamics are extracted from half-cell impedance spectra between 1 kHz and 10 Hz, including the ionic conductivity of the SEI κ_{SEI}, its surface site density Γ_{SEI}, which captures anode kinetics, its interfacial double-layer capacitances $C_{DL,sSEI}$ and $C_{DL,SEIe}$, the cathode reaction rate constant $k_{0,c}$, and the cathode double-layer capacitance $C_{DL,c}$.

The chemical potentials and Redlich-Kister coefficients related to the open circuit potentials of both electrodes are adopted from our previous work.[50] The electrolyte properties are again approximated

Table 2. Summary of the parameterization steps, including estimated model parameters and utilized experiments for the initial model parameterization for cycle 0 and the update of aging-sensitive model parameters for cycles 50 and 100.

Step	Data	Parameters (initial)	Parameters (update)
Direct calculation	Lithium loss during formation	d_{SEI}	–
I	C/10 discharge	$c_{a,0}$, $c_{c,0}$, $c_{a,max}$, $c_{c,max}$	d_{SEI}, $D_{s,c}$
II	1C, 2C discharge	τ_a, τ_c, $D_{s,c}$	τ_a, τ_c, $D_{s,c}$
III	EIS	κ_{SEI}, Γ_{SEI}, $C_{DL,sSEI}$, $C_{DL,SEIe}$, $k_{0,c}$, $C_{DL,c}$	κ_{SEI}, Γ_{SEI}, $C_{DL,sSEI}$, $C_{DL,SEIe}$, $k_{0,c}$, $C_{DL,c}$

Batteries & Supercaps

Research Article
doi.org/10.1002/batt.202400023

Chemistry Europe
European Chemical
Societies Publishing

with empirical polynomials by Landesfeind et al. for 1 M $LiPF_6$ in EC:EMC 3:7 (w:w).[60] The basic parameter set that is used for the simulation of all cells is given in the SI, Table S6. The adjusted model parameters for one cell each of the formation procedures F@C/10, F@C/2, and F@C/2$_{3.7\,V}$ at 20°C are summarized in the SI, Table S7, for cycles 0, 50, and 100.

All simulations were performed with MATLAB version 2021b, using the solver ode15s. The cell discretization comprises twelve representative active material particles for the anode and cathode. Each particle consists of four volume elements. The separator is divided into thirteen volume elements.

Results and Discussion

The following analysis of the cell formation study is divided in three parts. First, the effect of the applied cell formation procedure and temperature on the cell performance is analyzed. Afterward, the experimental data of the best-performing cell is analyzed in more detail to better understand the origin of the formation-induced performance improvement compared to the reference, i.e., the C/10 formation at 20°C. Finally, model-based cell and SEI modeling is used to identify the key cell properties that lead to this enhanced cell performance.

Effect of Formation on Cell Performance

Figure 1a shows the C/10 discharge, and Figure 1b the 2C discharge and charge capacities for formation procedures F@C/10, F@C/2, and F@C/2$_{3.7\,V}$ and formation temperatures of 20°C, 35°C, and 50°C. The slow formation F@C/10 at 20°C is used as a reference to facilitate the comparison between the different formation variations. The discussion of higher C-rates is omitted, as charge capacities at 3C already fall below 20% of their theoretical values (see SI, Figure S8). Part of this performance drop at high C-rates can be attributed to the utilized 220 μm separator in the three-electrode setup.

For C/10 discharge, it can be seen that the applied formation procedure and temperature have only a small effect on the initial capacity. For instance, the shallow formation cycling F@C/2$_{3.7\,V}$ at 20°C shows the highest capacity in the formation study (+6%). However, the same procedure applied at 50°C features the lowest capacity (−3%). A general trend between capacity and formation temperature independent of formation procedure cannot be observed.

For 2C discharge, the performance differences due to formation are much more significant. Any formation variation matches or exceeds the capacity of the reference procedure. In fact, the reference procedure F@C/10 applied at formation temperatures of 35°C and 50°C can already offer a 24% and 13% higher capacity, respectively. However, this clearly lags behind F@C/2$_{3.7\,V}$ at 20°C, which shows a discharge capacity improvement of 41%. Interestingly, F@C/2 at 20°C resembles more the performance characteristics of the reference formation F@C/10. This indicates that the omission of the full depth of discharge between the first and second formation cycle is critical for superior fast discharge capability. Vice versa, the shallow formation cycling F@C/2$_{3.7\,V}$ at 50°C just meets the reference capacity. Here, the full depth of discharge in F@C/2 seems to be beneficial, resulting in a 29% performance improvement compared to the reference.

For 2C charge, only F@C/2$_{3.7\,V}$ at 20°C can substantially outperform the reference formation. Elevated formation temperatures seem to be disadvantageous. Some cells even perform significantly worse than the reference case. For instance, the shallow formation F@C/2$_{3.7\,V}$ at 50°C underperforms by 24%. The slow formation F@C/10 at 50°C shows similar losses. In contrast, the shallow formation procedure applied at 20°C can outperform the reference formation by 63%. Similar to 2C discharge, cycling in the upper cell voltage regime seems critical. Again, F@C/2 with a full depth of discharge does not show this significant improvement. It offers only an 11% increase.

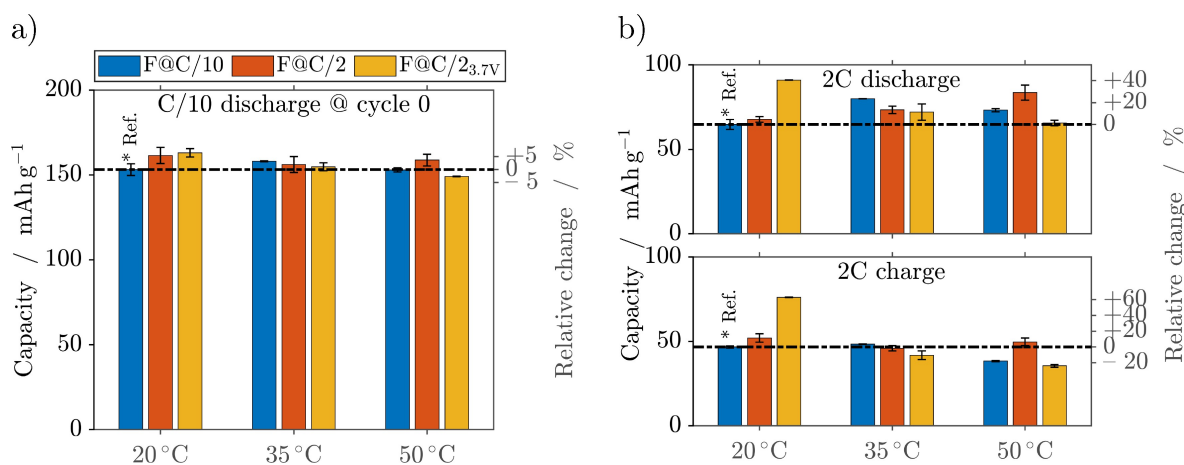Overall, the results show that elevated formation temperatures of 35°C and 50°C can boost the 2C discharge perform-

Figure 1. Comparison of a) C/10 discharge and b) 2C discharge and 2C charge capacities directly after formation as a function of formation procedure and formation temperature. The indicated standard deviations are based on two cells for each formation variation. The dashed-dotted line indicates the performance of the formation F@C/10 at 20°C directly after formation, which is used as the reference (marked by *).

Batteries & Supercaps

Research Article
doi.org/10.1002/batt.202400023

Chemistry
Europe
European Chemical
Societies Publishing

ance by up to 29% while maintaining a comparable C/10 discharge capacity. Although this cannot match the 41% capacity improvement for 2C discharge of F@C/2$_{3.7V}$ at 20°C, it suggests that elevated formation temperatures, e.g., by external temperature control or self-heating in large-format cells, can offer discharge performance improvements over the slow reference formation at 20°C. However, when the fast charge behavior is also considered, increased formation temperatures become less appealing as discharge improvements do not necessarily translate into better charge performance. This demonstrates again that the discharge capacity alone is not a reliable indicator of charge performance. Cells with similar discharge characteristics can have a strongly different fast charge capacity.[61] As a result, a comprehensive understanding of the effect of cell formation is not possible based on the commonly reported discharge capacity along aging.

When An et al. reported a benefit of shallow formation cycling compared to the standard full depth-of-discharge cycling, they observed an improvement in capacity retention for cycling at 1C along 1,300 cycles and a major reduction in cell formation time.[21] To assess the onset of cell behavior changes, Figure 2 shows the cell characteristics for all formation variations after 100 cycles. For simplicity, this cycle count omits all cycles from the applied cell characterization procedure.

For C/10 discharge, the capacities of all cells decrease and approach roughly the same value for formation at 20°C and 35°C. As a result, the initially higher capacity for F@C/2$_{3.7V}$ at 20°C is lost over the first 100 cycles. For formation at 50°C, F@C/10 and F@C/2$_{3.7V}$ experience an even faster capacity loss and underperform the reference formation by roughly 5%.

Similar to the cell characteristics directly after cell formation, the shallow formation cycling F@C/2$_{3.7V}$ at 20°C still outperforms for 2C discharge and charge by 25% and 46%, respectively. Compared to the cell behavior directly after formation, the total capacity remains roughly the same for the discharge direction. The relative benefit is reduced because the reference performed better after 100 cycles than immediately

after formation. For the charge direction, the relative benefit decreased due to an absolute decline in capacity.

Eventually, the results show that F@C/2$_{3.7V}$ at 20°C is unique in delivering substantial performance benefits for both fast discharge and fast charge. Due to the overall impaired cell performance at elevated formation temperatures, the following analysis will focus on the origin of performance differences for formation at 20°C. Possible reasons for the performance disadvantages at elevated formation temperatures are analyzed in the SI, Sections S1.2 and S1.3, considering anode half-cell potentials during formation and EIS data.

Detailed Experimental Analysis of Best-Performing Cell

The following discussion focuses on the best-performing cell, i.e., the cell after the shallow formation cycling F@C/2$_{3.7V}$ at 20°C. Here, the comparison with the formation F@C/10 and F@C/2 at 20°C allows to assess the effect of the applied C-rate and the depth of discharge, respectively.

Figure 3 shows the C-rate dependence of the cathode and anode half-cell potentials for all formation procedures. Although this does not allow for a direct quantification of differences in performance-limiting processes, it still enables a qualitative assessment of the formation impact. Importantly, the 220 μm thick separator, while reducing geometry-induced artifacts in the half-cell EIS data, is about one order of magnitude thicker than commercially relevant separators.[62,63] This deteriorates cell performance at elevated C-rates due to extended transport pathways. The additional potential drop between the reference electrode and the anode causes an offset in the measured anode half-cell potential from the true potential at the anode surface, which is indicative of lithium plating.[64] The canonical threshold of 0 V vs. Li/Li$^+$ is also only a first indicator of lithium plating, considering its concentration dependence.[65] As such, the negative anode potential during 1C and 2C charge in Figure 3b cannot be clearly identified as lithium plating without further experiments.
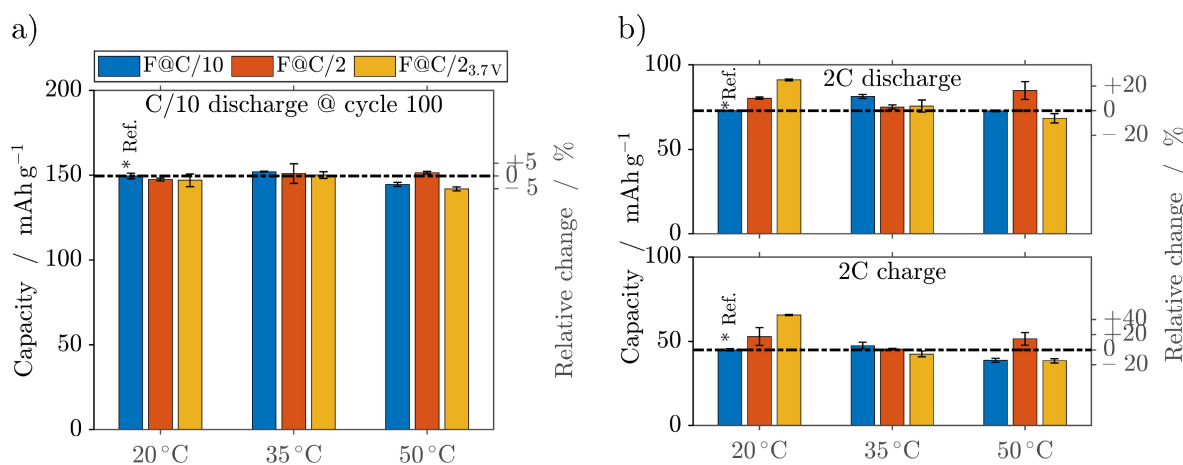

Figure 2. Comparison of a) C/10 discharge and b) 2C discharge and 2C charge capacities after 100 cycles as a function of formation procedure and formation temperature. The indicated standard deviations are based on two cells for each formation variation. The dashed-dotted line indicates the performance of the formation F@C/10 at 20°C after 100 cycles, which is used as the reference (marked by *).
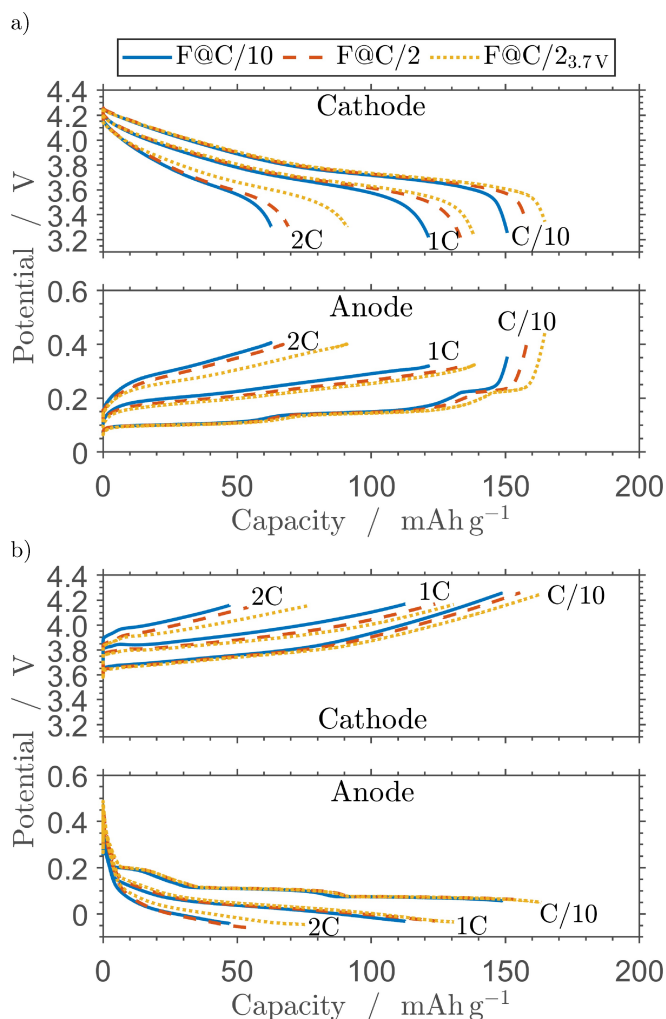
Batteries & Supercaps

Research Article
doi.org/10.1002/batt.202400023

**Chemistry
Europe**
European Chemical
Societies Publishing

Figure 3. Cathode and anode half-cell data from the C-rate test directly after formation for all three formation procedures at 20 °C. The half-cell potentials are shown for C-rates of C/10, 1C, and 2C in a) discharge and b) charge direction.

The discharge capacity at C/10 in Figure 3a changes with formation procedure, indicating either a formation-dependent loss of lithium inventory, a change in the usable active material, or likely a combination of both. This is supported by a differential voltage analysis of the C/10 discharge data (see SI, Figure S2). Herein, the characteristic features are the same for all formation procedures. However, they are visible at shifted positions, which suggests a change in the accessible active material of anode and cathode.[66,67]

For 2C discharge, notable differences in the anode and cathode half-cell potentials can be observed between the investigated formation procedures. The anode half-cell potential is notably lower and the cathode half-cell potential is significantly higher for F@C/2$_{3.7\,V}$. This suggests changes in mass transport or reaction kinetics in both electrodes.

Figure 3b shows the cathode and anode half-cell potential for the charge direction at C-rates of C/10, 1C, and 2C. At the lowest investigated C-rate of C/10, a different capacity can be seen again. At higher C-rates, differences in the cathode

overpotential become obvious. In combination with the observed differences between the formation procedures in Figure 3a for the discharge direction, this strongly suggests that both the anode and the cathode must have been affected by the applied formation procedure in terms of mass transport, reaction kinetics, or a combination of both.

Figure 4a shows the anode potential during cell formation at 20 °C as a function of time. The shallow formation cycling F@C/2$_{3.7\,V}$ takes roughly 6 h. F@C/2 features a process duration of about 8.5 h. The reference formation F@C/10 requires about 37 h. It can also be seen that the best-performing shallow formation cycling F@C/2$_{3.7\,V}$ maintains a low anode potential < 200 mV for an extended time. There are multiple reasons why this potential range could be beneficial. Although SEI growth continues in the discharge direction, it is less pronounced than in the charge direction.[35,68] By avoiding a complete discharge, SEI formation can continue at a low anode potential, which likely leads to a more dense and stable SEI.[15,26,27] Partially discharging reduces volume changes of the active material, and thus also mechanical stress on the newly formed SEI. This can help minimize the SEI and particle fracture probability, limiting subsequent SEI growth at such exposed surface sites.[69] Furthermore, molecular dynamics simulation studies have shown that the electrode potential significantly influences the composition of the electrolyte close to the graphite surface.[70] This likely contributes to the critical importance of the anode potential during cell formation for a well-protective yet not performance-inhibiting SEI.
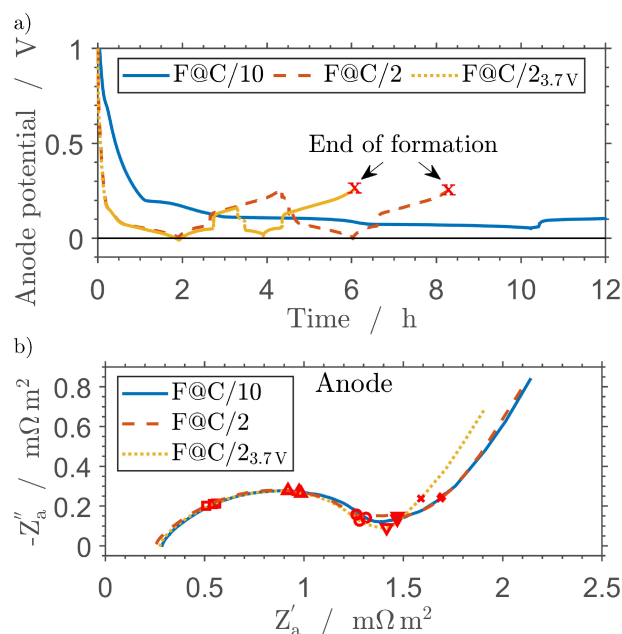

Figure 4. Detailed insights into different formation procedures at 20 °C. a) Anode half-cell potentials during formation. The end of the formation procedures F@C/2 and F@C/2$_{3.7\,V}$ is highlighted with red markers. For F@C/10, the cell formation takes more than 37 hours. b) Anode half-cell impedances at a cell voltage of 3.7 V after formation. Five frequencies are highlighted with red markers: 1 kHz ($\square$), 100 Hz ($\triangle$), 10 Hz ($\circ$), 1 Hz (∇), and 0.1 Hz ($\times$).

Apart from SEI growth and its effect on cell performance, none of the formation variations in Figure 4a shows an anode potential notably below 0 V vs. Li/Li$^+$, avoiding safety-critical lithium plating.[71] However, a recent study found that small amounts of plated lithium during formation have no significant effect on thermal cell safety and capacity retention during cycling.[72] Eventually, this provides headroom for a further reduction of formation time, e.g., via a model-based fast charge optimization.[25]

The anode half-cell impedance spectra in Figure 4b are very similar for all three formation procedures at 20 °C. Such similarity indicates a rather small or negligible effect of the formation procedure on the interfacial and bulk properties of the SEI. Yet, the cell performance was impacted by the applied formation variation. This points to formation-induced differences in effective transport properties for lithium-ions. Notable changes in anode and cathode half-cell potentials during 2C charge and discharge (see Figure 3), along with negligible changes in anode impedance and quite similar full-cell impedance (see SI, Figure S1), support the claim of formation-induced differences in transport properties.

Model-Based Analysis of Performance-Enhancing Cell Properties

Model-based cell diagnostics is valuable for gaining detailed insights into physically meaningful cell properties from non-destructive measurements. However, mere parameter values and their evolution along aging do not provide an intuitive understanding of why a cell behaves differently. The following discussion will start with a brief assessment of performance-sensitive model parameters. Afterward, the actual parameter values and their trend along aging are analyzed, focusing on the best-performing cell after formation F@C/2$_{3.7 V}$ at 20 °C.

The parameters in the employed cell and SEI model can be broadly divided into five categories: i) active material-related, i.e., initial and maximum lithium concentrations, ii) transport-related, i.e., solid diffusion in the active material and transport in the electrolyte phase, iii) charge-transfer-related, i.e., kinetics at the particle and SEI surface, iv) SEI-related, i.e., SEI thickness and ionic conductivity, and v) dynamics-related, i.e., double-layer capacitances. The earlier introduced parameterization procedure contains model parameters from all five categories. It is important to differentiate between model parameters that can be identified based on the available measurement data and those that can also explain differences in the discharge behavior. For instance, a double-layer capacitance can significantly influence the cell voltage during rapid dynamic operation in the range of 1 Hz to 100 Hz. Thus, it can be identified from EIS, but it has no impact on the 2C discharge capacity. A sensitivity analysis (see SI, Section S2.1) provides a deeper understanding of the effect of individual model parameters on the discharge behavior. The following discussion will focus on those ten parameters that are notably performance-sensitive. The identified parameter values, including the ones that are not performance-sensitive, are given in the SI, Table S7. First, the

initial and maximum lithium concentrations in the cathode and anode active material are analyzed. Afterward, the initial cell state and its evolution during aging are examined in terms of SEI thickness d_{SEI}, anode tortuosity τ_a and cathode tortuosity τ_c, cathode solid diffusion $D_{s,c}$, and anode and cathode reaction kinetics, represented by Γ_{SEI} and $k_{0,c}$, respectively.

The initial and maximum lithium concentrations in the anode and cathode active material are adjusted directly after formation based on C/10 discharge data. The estimated ratio of initial and maximum concentrations, i.e., the lithiation degrees at the beginning of discharge, is fairly similar for all formation procedures: they deviate no more than $\pm 1.6\%$ from the reference F@C/10. However, the maximum concentrations for the anode and cathode active material for F@C/2$_{3.7 V}$ are estimated to be 6.6% and 10.9% higher compared to the reference formation F@C/10, respectively. This can explain mainly the about 6% higher C/10 discharge capacity, with a similar relative improvement at higher C-rates (see SI, Figure S9). As such, these parameters alone cannot explain the 41% increase in 2C discharge capacity for F@C/2$_{3.7 V}$. On the electrode-level, these parameter changes suggest that more active material and thus also more lithium inventory seem to be accessible. This is supported by the differential voltage analysis of the half-cell potentials during C/10 discharge (see SI, Figure S2).

In general, a smaller maximum lithium concentration in either anode or cathode active material may be related to an increased amount of active material that is isolated from the ionic or electronic network, e.g., due to blocked pores by side reaction products. However, a change in the lithiation-dependent solid diffusivity and especially its decline for high lithiation levels[73] or a change in reaction kinetics[47] could also contribute to an apparent change in the available active material. A differential voltage analysis at notably lower C-rates than C/10 would allow to reduce the effect of these processes. Additional characterization measurements, like the galvanostatic intermittent titration technique (GITT) for the analysis of solid diffusivity,[74] and inductively coupled plasma optical emission spectroscopy (ICP-OES) for the investigation of average cathode lithiation or even its distribution across single cathode particles,[75] could help to reach a definitive conclusion regarding the change in accessible active material. In any case, the parameter estimates highlight that both the anode and cathode are affected positively by the shallow formation procedure F@C/2$_{3.7 V}$ compared to both F@C/10 and F@C/2.

Figure 5 shows the six performance-sensitive model parameters for the initial and aged cell states. First, we will explore the initial cell states, as understanding these will provide deeper insights into the observed formation-induced performance differences. Herein, the initial SEI thickness d_{SEI} differs among the three formation procedures, with a 20% thinner SEI for the shallow formation cycling F@C/2$_{3.7 V}$ compared to the reference F@C/10. Differences in the SEI thickness have two implications: an initial capacity loss and a change in anode porosity due to a different total SEI volume. Nonetheless, the initial differences in this parameter cannot explain a notable part of the 41% increase in 2C discharge capacity (see SI, Figure S11a).
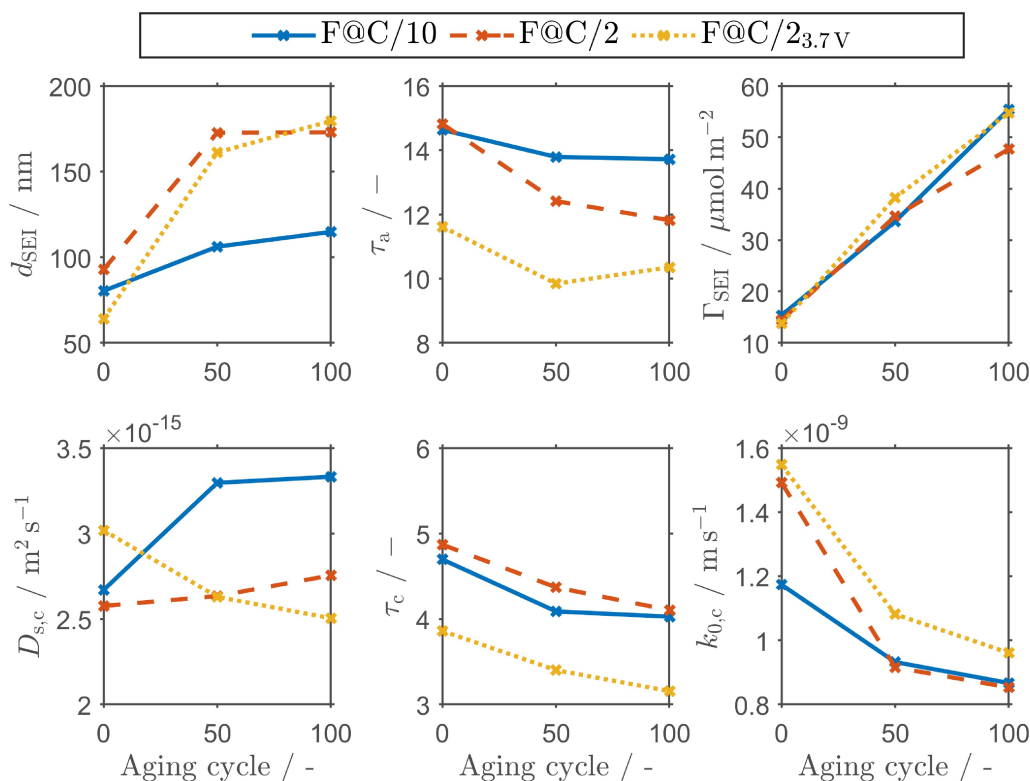
Batteries & Supercaps

Research Article
doi.org/10.1002/batt.202400023

Chemistry Europe
European Chemical
Societies Publishing

Figure 5. Performance-sensitive parameter estimates from the model-based cell diagnosis for all three formation procedures at 20 °C along the first 100 cycles. The first row shows the evolution of the SEI thickness d_{SEI}, the anode tortuosity τ_a, and the surface site density of the SEI Γ_{SEI}. Notably, τ_a serves as a scaling factor for effective transport properties within the anode electrolyte phase, while Γ_{SEI} maps anode reaction kinetics. The second row shows the cathode solid diffusion coefficient $D_{s,c}$, the cathode tortuosity τ_c, which serves as a scaling factor for effective transport properties within the cathode electrolyte phase, and the cathode reaction rate constant $k_{0,c}$.

The anode tortuosity τ_a, and thus a transport-related parameter, was found to be about 20 % lower, i.e., better, for the shallow formation cycling F@C/2$_{3.7\,V}$ compared to both F@C/10 and F@C/2. If the initially formed SEI by F@C/2$_{3.7\,V}$ had either less volume in total, i.e., a higher electrode porosity, or a more favorable structure, i.e., a lower electrode tortuosity, effective transport in the electrolyte phase would improve. As such, formation-induced changes in τ_a may be seen as a secondary effect of surface film formation. Although it is not possible to pinpoint the major cause or distinguish between changes in porosity and tortuosity without additional experiments, it can be clearly stated that the effective transport properties in the anode electrolyte phase are affected by the applied formation procedure.

The anode tortuosity can explain part of the performance difference at elevated C-rates (see SI, Figure S10a). Thus, it is worthwhile to discuss formation-induced tortuosity changes in more detail and relate them to findings in literature. As a surface film, the SEI inherently alters the microstructure of an electrode. For instance, a cryo-TEM study on a carbonaceous electrode found that a thin SEI nucleates at first, evolving into i) a compact SEI with a high ratio of inorganic, well-passivating components and ii) an extended SEI with a thickness of hundreds of nanometers.[44] Nano-resolution X-ray computed tomography revealed substantial microstructural changes in an anode along cycling, featuring 50 % less pore volume within a

cycle-aged compared to a pristine electrode from a commercial cell.[76] This change was attributed to ongoing SEI growth, i.e., the accumulation of electrolyte decomposition products within the pore volume. In silicon anodes, extensive SEI growth could also be identified as a major limitation for transport within the bulk electrolyte.[77] In graphite-silicon composite electrodes, a highly heterogeneous SEI thickness and a displacement of the carbon-binder domain by the SEI could be observed.[78] For active material with poor electrical conductivity, this may trigger a rapid performance deterioration due to the collapse of the conductive network.[79] Overall, this emphasizes the crucial role of a dense and protective SEI in ensuring consistent cell performance over the long term. If the SEI extends substantially into the bulk electrolyte, it effectively deteriorates lithium-ion transport within the pore volume. Our model-based analysis of the electrochemical characterization measurements suggests strongly that the transformation of the microstructure of a pristine electrode already starts during the cell formation process, i.e., before any cycle aging.

The question remains as to why SEI growth could result in a different anode tortuosity τ_a for different formation procedures. The lower tortuosity for the shallow formation cycling F@C/2$_{3.7\,V}$ compared to the full depth-of-discharge cycles in F@C/2 may be related to the extended duration at low anode potentials, which is associated with a more stable and dense SEI.[15,26,27] However, minimizing the time at high anode potentials seems

Batteries & Supercaps

Research Article
doi.org/10.1002/batt.202400023

Chemistry
Europe

European Chemical
Societies Publishing

insufficient for a beneficial tortuosity change. Otherwise, there should be a significant difference between F@C/2 and the much slower formation procedure F@C/10. In this context, an experimental study demonstrated that the nascent SEI can be partially oxidized during discharge, leading to the decomposition into both gaseous and solid products.[42] This could explain why shallow formation cycles result in improved cell characteristics. Without substantial oxidation and a subsequent new formation of the SEI, its initial structure could remain largely intact, potentially preventing additional SEI growth and reducing its impact on transport within the pore network. To the same end, the reduced depth of discharge causes less volume change in the active material, which could result in less mechanical stress and a lower fracture probability for the nascent SEI during formation.

The surface site density of the SEI Γ_{SEI}, which maps anode reaction kinetics, deviates slightly between the formation procedures. The parameter is 6% lower for F@C/2 and about 10% lower for F@C/2$_{3.7V}$ compared to the reference formation. However, a deviation of this magnitude has a negligible effect on the discharge performance (see SI, Figure S11c), and thus cannot explain formation-induced performance deviations. This was already expected from the similar anode half-cell impedance in Figure 4b. Combined with the differences in anode tortuosity, this supports the common understanding of the SEI as a two-layered structure with a more porous and organic outer layer and a predominately dense and inorganic layer at the particle surface.[80–82] If the outer SEI layer was sufficiently porous, lithium-ion transport would resemble that of the bulk electrolyte phase. In that case, only the inner layer of the SEI would be visible in EIS measurements as no charge transfer reaction would take place at the outer SEI layer. This could explain differences in electrolyte-level transport and yet allow for similar anode reaction kinetics.

On the cathode side, the solid diffusion coefficient $D_{s,c}$ is about 13% higher for the shallow formation cycling F@C/2$_{3.7V}$ and about 4% lower for F@C/2 compared to F@C/10. Similar to the anode tortuosity, the critical factor for an improvement does not seem to be the applied C-rate. Otherwise, F@C/2 and F@C/2$_{3.7V}$ should feature similar parameter values. Instead, the omission of the full depth of discharge, and thus an extended uninterrupted duration at high potentials, seems critical for improved solid diffusivity. This could be attributed, e.g., to beneficial changes in the grain boundaries, which are essential for the effective diffusivity inside the active material particles,[83] or a change in surface film composition and porosity, which may affect transport into the underlying active material.[84,85] Mechanical degradation of the active material particles is unlikely to contribute notably to changes in the solid diffusivity as it develops over hundreds of cycles.[37,86] A clear identification of the primary cause for the diffusion improvement is not possible based on the performed experiments. Nonetheless, this parameter has a notable effect on the observed differences in the 1C and 2C discharge capacity (see SI, Figure S10d). A publication on coated cathode active material used the suitable term "apparent diffusion coefficient", which summarizes well that multiple factors affect its value beyond bulk diffusion.[87]

The cathode tortuosity τ_c was also affected by the applied formation procedure. The values for F@C/10 and F@C/2 are fairly similar, with a less than 4% higher tortuosity for F@C/2. The shallow formation without full depth of discharge F@C/2$_{3.7V}$ features an 18% lower tortuosity, which indicates beneficial changes in the microstructure of the cathode. Changes of this magnitude have a significant effect on the discharge performance at 2C but only a small effect at 1C (see SI, Figure S10b). This highlights that cell formation affects not only particle-level transport, i.e., solid diffusivity, but also electrode-level transport, i.e., electrode tortuosity. As the investigated formation procedures comprise only two cycles at moderate C-rates of up to C/2, substantial particle cracking and a corresponding change in electrode microstructure, like during cycle-aging, would not be expected.[88] This points all the more at a different surface film formation on the cathode side. In general, a higher cell voltage promotes electrolyte decomposition and thus surface film formation.[89,90] However, it has also been reported that the cathode surface film growth during discharge was much more pronounced compared to maintaining a high voltage.[91] This may explain part of the benefit of the shallow formation cycling. Furthermore, cross-talk between anode and cathode may affect the final surface film properties.[90] As such, the improved cathode tortuosity for F@C/2$_{3.7V}$ may be no coincidence, considering the equally beneficial anode tortuosity. In this context, a study on fast charging demonstrated that an artificial SEI on graphite could substantially improve the long-term capacity retention.[92] This also poses the question of whether the improved aging behavior and performance in their study originated only from improved anode properties or also a lack of cross-talk between anode and cathode due to the artificial SEI. Eventually, the performed C-rate tests and EIS data in this work cannot answer i) if only the extended uninterrupted duration at high cathode potentials or ii) if also the favorable SEI formation on the anode side causes the significantly improved cathode performance.

The cathode reaction rate constant $k_{0,c}$ is lowest for the reference formation. It is about 27% and 32% higher for F@C/2 and F@C/2$_{3.7V}$, respectively. This could imply a larger electrochemically active surface area or an altered surface composition. However, parameter differences of this magnitude have only a small effect at elevated C-rates, primarily influencing the cell voltage and not the discharge capacity (see SI, Figure S11d).

Finally, the parameter changes during aging are discussed. The SEI growth continues for cycles 50 and 100, but it seems to decelerate substantially between cycle 50 and 100 for F@C/2 and F@C/2$_{3.7V}$. The slow formation F@C/10 shows a much smaller increase in SEI thickness, which suggests a better passivating SEI. However, this seemingly better passivation capability was achieved with a higher initial capacity loss.

Apart from an increase of the SEI thickness, steady improvements in anode reaction kinetics (Γ_{SEI}) suggest an ongoing transformation of this surface film. However, this improvement has only a marginal effect on the cell voltage during fast discharge, yet it is clearly identifiable from the anode half-cell impedance data. Similar changes take place for the not performance-limiting double-layer capacitances at the inner

Batteries & Supercaps

Research Article
doi.org/10.1002/batt.202400023

Chemistry Europe
European Chemical
Societies Publishing

and outer interface of the SEI ($C_{DL,sSEI}$, $C_{DL,SEle}$), which support the expectation of either an increase in electrochemically active surface area, e.g., due to particle cracking,[93] or a change in SEI composition and structure. Such surface film alterations could originate from the further reduction of SEI components[13] or cross-talk with electrolyte oxidation products from the cathode.[40,94] A partial surface film decomposition could also explain the decrease of the anode tortuosity for all cells between cycle 0 and 50. Although this trend continues between cycle 50 and 100 for F@C/10 and C/2, the anode tortuosity for F@C/2$_{3.7V}$ already increases slightly. Given the better charge and discharge performance for F@C/2$_{3.7V}$, aspects like the total charge throughput during cycling may contribute to the observed parameter increase. Given the absence of a consistent parameter trend for all formation procedures over 100 cycles, conducting extended cycling experiments becomes even more important to assess the long-term effect of cell formation on dominant aging mechanisms.

The trend for the cathode solid diffusivity $D_{s,c}$ is unique for each cell. It improves between cycle 0 and 100 by about 25% for F@C/10 and 7% for F@C/2, but it declines about 18% for F@C/2$_{3.7V}$. As already discussed for the initial cell state, our simplified model cannot pinpoint the root cause for changes in the apparent solid diffusivity using discharge curves and impedance data. An in-depth understanding of the long-term effect of cell formation on the aging behavior would require further experiments. A detailed characterization of the surface species[85] and an analysis of the mechanical degradation of the active material particles would be especially relevant.[86]

The cathode tortuosity τ_c decreases, i.e., improves, by at least 20% for all cells during aging. Similar to the anode tortuosity, imaging techniques, like nano-resolution X-ray computed tomography, could help to advance the understanding of the root cause of this improvement.[76] Furthermore, by using a cross-talk blocking separator, it would be possible to discriminate the impact of electrode cross-talk from the intrinsic effect of the formation process on transport processes within the cathode.[95] A detailed analysis of changes in the electrolyte composition could provide further insights.[96]

In contrast to the anode, the cathode reaction rate constant $k_{0,c}$ deteriorates for all formation procedures during cycling. Independent of the initial value, it seems to asymptotically approach a similar value for all formation procedures after 100 cycles. This suggests that the electrochemically active surface of the cathode particles may have reached a more equilibrated chemical or mechanical state.

Overall, the study revealed a multitude of changes in parameters due to formation but also aging. This raises several intriguing questions about the underlying causes and invites further analysis, as suggested above. Moreover, it is important to note that 100 cycles only mark the beginning of cell aging. Further experiments over the full lifetime and in a commercially-relevant cell format are necessary to verify if, or rather how long, the estimated parameter trends continue and how long the fast charge/discharge benefit of the shallow formation F@C/2$_{3.7V}$ at 20°C is maintained. High-precision coulometry could prove to be a valuable tool for the rapid screening of formation protocols to assess aging within weeks instead of months.[97]

Conclusions

In this study, we found a substantial impact of the applied cell formation procedure and temperature on the fast charge/discharge capability of NMC622│G raphite cells. For elevated formation temperatures of 35°C and 50°C, some formation procedures were able to outperform the reference formation F@C/10 at 20°C in terms of 2C discharge capacity by up to 29%. However, for 2C charge, these formation variations fell short of, let alone exceed, the performance of this reference. This implies that a formation temperature of 20°C is essential to realize well-balanced performance characteristics with the investigated cell chemistry and design, underscoring the significance of this process parameter.

The experiments revealed that shallow formation cycling F@C/2$_{3.7V}$ at 20°C can boost the cell performance for 2C discharge and 2C charge by 41% and 63%, respectively. With a full depth of discharge, the formation procedure F@C/2 did not show significant performance gains. This suggests that the extended, uninterrupted time at a low anode potential, a high cathode potential, or a combination of both is critical for superior performance. Eventually, this adds to the reported benefit of the time-efficient shallow formation procedures by An et al., who demonstrated better capacity retention during long-term cycling.[21]

The model-based analysis of the best-performing cell after formation with F@C/2$_{3.7V}$ at 20°C and its differences to the other formation procedures could provide deeper insights into potential structural changes within the cell. It could be shown that its performance benefit originated from both the anode and the cathode. Notably, the initial SEI thickness and anode reaction kinetics were similar for all investigated formation procedures. Cathode reaction kinetics improved, but did not substantially alter the 2C discharge capacity. Instead, improved effective transport in the anode and especially the cathode electrolyte phase in combination with an enhanced cathode solid diffusivity were identified as the primary drivers for the superior cell performance.

We presented an in-depth discussion of possible causes. The anode-side transport improvement may be related to a different structure or composition of the SEI. Here, the shallow formation cycling may allow for SEI growth with a reduced impact on the electrode microstructure: low anode potentials favor the formation of a dense and stable SEI, and incomplete discharge may minimize the mechanical stress and the reported restructuring of the formed SEI. For the cathode, improved effective transport properties in the solid and electrolyte phase may also be attributed to a beneficial surface film formation. Eventually, further research will be necessary to expand the understanding of surface film growth on the cathode side, comprising dedicated half- and full-cell studies on cross-talk between anode and cathode for different formation procedures

Batteries & Supercaps

Research Article
doi.org/10.1002/batt.202400023

Chemistry
Europe

European Chemical
Societies Publishing

and electrolyte compositions. Here, the use of a cross-talk blocking separator may prove helpful.[95]

In terms of cell degradation, the model-based cell diagnosis highlighted that some cell properties, like the SEI thickness and anode tortuosity, still evolve after formation but stabilize between cycles 50 and 100. Other parameters, like the surface site density of the SEI, display a fairly steady increase. Utilizing the presented model provided deep and unparalleled insights into formation-induced performance changes, circumventing the necessity for non-electrochemical, destructive measurements. While the model serves as a potent diagnostic aid, it is imperative to recognize the intricate effects of cell formation on both performance and aging. Understanding the long-term impact of different cell formation conditions, coupled with their knowledge-driven optimization, remains a complex endeavor. The sampling efficiency of data-driven optimization approaches might offer an edge in navigating this complexity.[98]

Supporting Information

The authors have cited additional references within the Supporting Information.[99–102] The abbreviations and symbols are defined in the Supporting Information.

Acknowledgements

Conflict of Interests

The authors declare no conflict of interest.

Data Availability Statement

The data presented in the manuscript are openly available in the KITopen repository at DOI: 10.35097/1872.
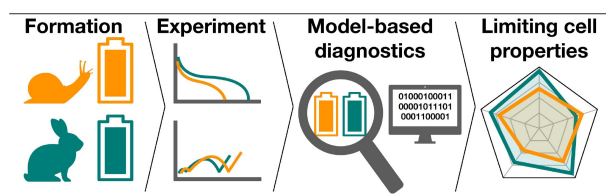
[1] T. Placke, R. Kloepsch, S. Dühnen, M. Winter, *J. Solid State Electrochem.* **2017**, *21*, 1939.

[2] A. W. Schäfer, S. R. H. Barrett, K. Doyme, L. M. Dray, A. R. Gnadt, R. Self, A. O'Sullivan, A. P. Synodinos, A. J. Torija, *Nat. Energy* **2019**, *4*, 160.

[3] C. Xu, Q. Dai, L. Gaines, M. Hu, A. Tukker, B. Steubing, *Commun. Mater.* **2020**, *1*, 99.

[4] L. Usai, J. J. Lamb, E. Hertwich, O. S. Burheim, A. H. Strømman, *Environ. Res. Infrastruct. Sustain.* **2022**, *2*, 011002.

[5] A. Kwade, W. Haselrieder, R. Leithoff, A. Modlinger, F. Dietrich, K. Droeder, *Nat. Energy* **2018**, *3*, 290.

[6] F. Duffner, L. Mauler, M. Wentker, J. Leker, M. Winter, *Int. J. Prod. Econ.* **2021**, *232*, 107982.

[7] P. A. Nelson, S. Ahmed, K. G. Gallagher, D. W. Dees, Modeling the Performance and Cost of Lithium-Ion Batteries for Electric-Drive Vehicles, Third Edition, Technical report, Argonne National Laboratory (ANL), Argonne, IL (United States) **2019**.

[8] Y. Liu, R. Zhang, J. Wang, Y. Wang, *iScience* **2021**, *24*, 102332.

[9] D. L. Wood, J. Li, S. J. An, *Joule* **2019**, *3*, 2884.

[10] S. Davidsson Kurland, *Environ. Res. Commun.* **2020**, *2*, 012001.

[11] A. Jinasena, O. S. Burheim, A. H. Strømman, *Batteries* **2021**, *7*, 1.

[12] A. Wang, S. Kadam, H. Li, S. Shi, Y. Qi, *npj Comput. Mater.* **2018**, *4*, 15.

[13] S. J. An, J. Li, C. Daniel, D. Mohanty, S. Nagpure, D. L. Wood, *Carbon* **2016**, *105*, 52.

[14] E. Peled, S. Menkin, *J. Electrochem. Soc.* **2017**, *164*, A1703.

[15] S. Zhang, M. S. Ding, K. Xu, J. Allen, T. R. Jow, *Electrochem. Solid-State Lett.* **2001**, *4*, 10.

[16] I. Rubio Lopez, M. J. Lain, E. Kendrick, *Batteries & Supercaps* **2020**, *3*, 900.

[17] H. H. Heimes, C. Offermanns, A. Mohsseni, H. Laufen, U. Westerhoff, L. Hoffmann, P. Niehoff, M. Kurrat, M. Winter, A. Kampker, *Energy Technol.* **2020**, *8*, 1900118.

[18] E. Brorein, M. Vulovic, B. Boswell, R. Zollo (Keysight Technologies, Inc.), US 2018/0164363 A1, **2018**.

[19] A. Noel, I. Zilberman (Crino GmbH), EP 3 971 544 A1, **2022**.

[20] F. Schomburg, B. Heidrich, S. Wennemar, R. Drees, T. Roth, M. Kurrat, H. Heimes, A. Jossen, M. Winter, J. Y. Cheong, F. Röder, *Energy Environ. Sci.* **2024**, *17*, 2686.

[21] S. J. An, J. Li, Z. Du, C. Daniel, D. L. Wood, *J. Power Sources* **2017**, *342*, 846.

[22] V. Müller, R. Kaiser, S. Poller, D. Sauerteig, *J. Energy Storage* **2018**, *15*, 256.

[23] C. Mao, S. J. An, H. M. Meyer, J. Li, M. Wood, R. E. Ruther, D. L. Wood, *J. Power Sources* **2018**, *402*, 107.

[24] F. Röder, V. Laue, U. Krewer, *Batteries & Supercaps* **2019**, *2*, 248.

[25] R. Drees, F. Lienesch, M. Kurrat, *J. Energy Storage* **2021**, *36*, 102345.

[26] D. Lu, M. Xu, L. Zhou, A. Garsuch, B. L. Lucht, *J. Electrochem. Soc.* **2013**, *160*, A3138.

[27] P. M. Attia, S. J. Harris, W. C. Chueh, *J. Electrochem. Soc.* **2021**, *168*, 050543.

[28] H. B. Son, M.-Y. Jeong, J.-G. Han, K. Kim, K. H. Kim, K.-M. Jeong, N.-S. Choi, *J. Power Sources* **2018**, *400*, 147.

[29] V. A. Agubra, J. W. Fergus, *J. Power Sources* **2014**, *268*, 153.

[30] D. M. Seo, D. Chalasani, B. S. Parimalam, R. Kadam, M. Nie, B. L. Lucht, *ECS Electrochem. Lett.* **2014**, *3*, 3.

[31] S. K. Heiskanen, J. Kim, B. L. Lucht, *Joule* **2019**, *3*, 2322.

[32] M. Herstedt, A. M. Andersson, H. Rensmo, H. Siegbahn, K. Edström, *Electrochim. Acta* **2004**, *49*, 4939.

[33] F. M. Kindermann, J. Keil, A. Frank, A. Jossen, *J. Electrochem. Soc.* **2017**, *164*, E287.

[34] M. Heinrich, N. Wolff, N. Harting, V. Laue, F. Röder, S. Seitz, U. Krewer, *Batteries & Supercaps* **2019**, *2*, 530.

[35] A. M. Colclasure, K. A. Smith, R. J. Kee, *Electrochim. Acta* **2011**, *58*, 33.

[36] A. A. Tahmasbi, T. Kadyk, M. H. Eikerling, *J. Electrochem. Soc.* **2017**, *164*, A1307.

[37] A. Tahmasbi, M. Eikerling, *Electrochim. Acta* **2018**, *283*, 75.

[38] J. A. Gilbert, I. A. Shkrob, D. P. Abraham, *J. Electrochem. Soc.* **2017**, *164*, A389.

[39] S. Solchenbach, M. Metzger, M. Egawa, H. Beyer, H. A. Gasteiger, *J. Electrochem. Soc.* **2018**, *165*, A3022.

[40] C. Jayawardana, N. Rodrigo, B. Parimalam, B. L. Lucht, *ACS Energy Lett.* **2021**, *6*, 3788.

[41] B. S. Parimalam, A. D. MacIntosh, R. Kadam, B. L. Lucht, *J. Phys. Chem. C* **2017**, *121*, 22733.

[42] T. Liu, L. Lin, X. Bi, L. Tian, K. Yang, J. Liu, M. Li, Z. Chen, J. Lu, K. Amine, K. Xu, F. Pan, *Nat. Nanotechnol.* **2019**, *14*, 50.

[43] S. Y. Luchkin, S. A. Lipovskikh, N. S. Katorova, A. A. Savina, A. M. Abakumov, K. J. Stevenson, *Sci. Rep.* **2020**, *10*, 1.

Batteries & Supercaps

Research Article
doi.org/10.1002/batt.202400023

Chemistry Europe
European Chemical
Societies Publishing

[44] W. Huang, P. M. Attia, H. Wang, S. E. Renfrew, N. Jin, S. Das, Z. Zhang, D. T. Boyle, Y. Li, M. Z. Bazant, B. D. McCloskey, W. C. Chueh, Y. Cui, *Nano Lett.* **2019**, *19*, 5140.

[45] U. Westerhoff, K. Kurbach, F. Lienesch, M. Kurrat, *Energy Technol.* **2016**, *4*, 1620.

[46] T. P. Heins, N. Schlüter, S. T. Ernst, U. Schröder, *Energy Technol.* **2020**, *8*, 1900279.

[47] S. Gantenbein, M. Weiss, E. Ivers-Tiffée, *J. Power Sources* **2018**, *379*, 317.

[48] M. Gaberšček, *Nat. Commun.* **2021**, *12*, 19.

[49] V. Laue, F. Röder, U. Krewer, *J. Appl. Electrochem.* **2021**, *51*, 1253.

[50] D. Witt, F. Röder, U. Krewer, *Batteries & Supercaps* **2022**, *5*, e202200067.

[51] J. Landesfeind, J. Hattendorff, A. Ehrl, W. A. Wall, H. A. Gasteiger, *J. Electrochem. Soc.* **2016**, *163*, A1373.

[52] N. Kaden, N. Schlüter, R. Leithoff, S. Savas, S. Grundmeier, K. Dröder, *Processes* **2021**, *9*, 1851.

[53] M. Doyle, T. F. Fuller, J. Newman, *J. Electrochem. Soc.* **1993**, *140*, 1526.

[54] N. Legrand, S. Raël, B. Knosp, M. Hinaje, P. Desprez, F. Lapicque, *J. Power Sources* **2014**, *251*, 370.

[55] M. Gaberscek, J. Moskon, B. Erjavec, R. Dominko, J. Jamnik, *Electrochem. Solid-State Lett.* **2008**, *11*, 170.

[56] F. Single, B. Horstmann, A. Latz, *J. Phys. Chem. C* **2019**, *123*, 27327.

[57] H. J. Ploehn, P. Ramadass, R. E. White, *J. Electrochem. Soc.* **2004**, *151*, A456.

[58] E. W. C. Spotte-Smith, R. L. Kam, D. Barter, X. Xie, T. Hou, S. Dwaraknath, S. M. Blau, K. A. Persson, *ACS Energy Lett.* **2022**, *7*, 1446.

[59] O. Borodin, G. V. Zhuang, P. N. Ross, K. Xu, *J. Phys. Chem. C* **2013**, *117*, 7433.

[60] J. Landesfeind, H. A. Gasteiger, *J. Electrochem. Soc.* **2019**, *166*, A3079.

[61] D. Witt, D. Wilde, F. Baakes, F. Belkhir, F. Röder, U. Krewer, *Energy Technol.* **2021**, *9*, 2000989.

[62] M. Ender, J. Illig, E. Ivers-Tiffée, *J. Electrochem. Soc.* **2017**, *164*, A71.

[63] J. Costard, M. Ender, M. Weiss, E. Ivers-Tiffée, *J. Electrochem. Soc.* **2017**, *164*, A80.

[64] M.-T. F. Rodrigues, I. A. Shkrob, A. M. Colclasure, D. P. Abraham, *J. Electrochem. Soc.* **2020**, *167*, 130508.

[65] S. Carelli, W. G. Bessler, *J. Electrochem. Soc.* **2020**, *167*, 100515.

[66] M. Lewerenz, A. Marongiu, A. Warnecke, D. U. Sauer, *J. Power Sources* **2017**, *368*, 57.

[67] C. Pastor-Fernández, K. Uddin, G. H. Chouchelamane, W. D. Widanage, J. Marco, *J. Power Sources* **2017**, *360*, 301.

[68] F. Schomburg, R. Drees, M. Kurrat, M. A. Danzer, F. Röder, *Energy Technol.* **2022**, page 2200688.

[69] Y. Ali, N. Iqbal, S. Lee, *Int. J. Energy Res.* **2021**, *45*, 5293.

[70] J. Vatamanu, O. Borodin, G. D. Smith, *J. Phys. Chem. C* **2012**, *116*, 1114.

[71] T. Waldmann, B. I. Hogg, M. Wohlfahrt-Mehrens, *J. Power Sources* **2018**, *384*, 107.

[72] P. Münster, M. Diehl, J. E. Frerichs, M. Börner, M. R. Hansen, M. Winter, P. Niehoff, *J. Power Sources* **2021**, *484*, 229306.

[73] A. Jetybayeva, N. Schön, J. Oh, J. Kim, H. Kim, G. Park, Y. G. Lee, R. A. Eichel, K. Kleiner, F. Hausen, S. Hong, *ACS Appl. Energ. Mater.* **2022**, *5*, 1731.

[74] C.-H. Chen, F. Brosa Planella, K. O'Regan, D. Gastol, W. D. Widanage, E. Kendrick, *J. Electrochem. Soc.* **2020**, *167*, 080534.

[75] T. N. Kröger, M. J. Wölke, P. Harte, T. Beuse, M. Winter, S. Nowak, S. Wiemers-Meyer, *ChemSusChem* **2022**, *15*, 36.

[76] S. Frisco, A. Kumar, J. F. Whitacre, S. Litster, *J. Electrochem. Soc.* **2016**, *163*, A2636.

[77] A. L. Michan, G. Divitini, A. J. Pell, M. Leskes, C. Ducati, C. P. Grey, *J. Am. Chem. Soc.* **2016**, *138*, 7918.

[78] S. Müller, M. Lippuner, M. Verezhak, V. De Andrade, F. De Carlo, V. Wood, *Adv. Energy Mater.* **2020**, *10*, 1904119.

[79] O. Schmidt, F. Röder, *ACS Appl. Energ. Mater.* **2021**, *4*, 4845.

[80] F. Single, B. Horstmann, A. Latz, *Phys. Chem. Chem. Phys.* **2016**, *18*, 17810.

[81] Z. Liu, P. Lu, Q. Zhang, X. Xiao, Y. Qi, L. Q. Chen, *J. Phys. Chem. Lett.* **2018**, *9*, 5508.

[82] C. H. Lee, J. A. Dura, A. LeBar, S. C. DeCaluwe, *J. Power Sources* **2019**, *412*, 725.

[83] X. He, H. Sun, X. Ding, K. Zhao, *J. Phys. Chem. C* **2021**, *125*, 10284.

[84] S. Shi, Y. Qi, H. Li, L. G. Hector, *J. Phys. Chem. C* **2013**, *117*, 8579.

[85] M. J. Herzog, N. Gauquelin, D. Esken, J. Verbeeck, J. Janek, *ACS Appl. Energ. Mater.* **2021**, *4*, 8832.

[86] D. Goldbach, J. Gluch, T. Graf, M. Gaus, S. Käbitz, M. Zillmer, U. Krewer, *ChemElectroChem* **2023**, *202300353*.

[87] Y. Shi, M. Zhang, D. Qian, Y. S. Meng, *Electrochim. Acta* **2016**, *203*, 154.

[88] T. Bond, R. Gauthier, S. Gasilov, J. R. Dahn, *J. Electrochem. Soc.* **2022**, *169*, 080531.

[89] Y. Xie, H. Gao, J. Gim, A. T. Ngo, Z. F. Ma, Z. Chen, *J. Phys. Chem. Lett.* **2019**, *10*, 589.

[90] S. P. Kühn, K. Edström, M. Winter, I. Cekic-Laskovic, *Adv. Mater. Interfaces* **2022**, *9*, 2102078.

[91] J.-N. Zhang, Q. Li, Y. Wang, J. Zheng, X. Yu, H. Li, *Energy Storage Mater.* **2018**, *14*, 1.

[92] E. Kazyak, K. Chen, Y. Chen, T. H. Cho, N. P. Dasgupta, *Adv. Energy Mater.* **2022**, *12*, 2102618.

[93] H. Seng Chan, L. Bläubaum, D. Vijayshankar, F. Röder, C. Nowak, A. Weber, A. Kwade, U. Krewer, *Batteries & Supercaps* **2023**, *6*, e202300203.

[94] S. F. Schuster, T. Bach, E. Fleder, J. Müller, M. Brand, G. Sextl, A. Jossen, *J. Energy Storage* **2015**, *1*, 44.

[95] B. L. Rinkel, D. S. Hall, I. Temprano, C. P. Grey, *J. Am. Chem. Soc.* **2020**, *142*, 15058.

[96] R. Stockhausen, L. Gehrlein, M. Müller, T. Bergfeldt, A. Hofmann, F. J. Müller, J. Maibach, H. Ehrenberg, A. Smith, *J. Power Sources* **2022**, *543*, 231842.

[97] J. C. Burns, N. N. Sinha, D. J. Coyle, G. Jain, C. M. VanElzen, W. M. Lamanna, A. Xiao, E. Scott, J. P. Gardner, J. R. Dahn, *J. Electrochem. Soc.* **2011**, *159*, A85.

[98] P. M. Attia, A. Grover, N. Jin, K. A. Severson, T. M. Markov, Y.-H. Liao, M. H. Chen, B. Cheong, N. Perkins, Z. Yang, P. K. Herring, M. Aykol, S. J. Harris, R. D. Braatz, S. Ermon, W. C. Chueh, *Nature* **2020**, *578*, 397.

[99] M. Nie, J. Demeaux, B. T. Young, D. R. Heskett, Y. Chen, A. Bose, J. C. Woicik, B. L. Lucht, *J. Electrochem. Soc.* **2015**, *162*, A7008.

[100] F. L. E. Usseglio-Viretta, A. Colclasure, A. N. Mistry, K. P. Y. Claver, F. Pouraghajan, D. P. Finegan, T. M. M. Heenan, D. Abraham, P. P. Mukherjee, D. Wheeler, P. Shearing, S. J. Cooper, K. Smith, *J. Electrochem. Soc.* **2018**, *165*, A3403.

[101] A. M. Colclasure, R. J. Kee, *Electrochim. Acta* **2010**, *55*, 8960.

[102] S. Shi, P. Lu, Z. Liu, Y. Qi, L. G. Hector, H. Li, S. J. Harris, *J. Am. Chem. Soc.* **2012**, *134*, 15476.

RESEARCH ARTICLE

Formation | **Experiment** | **Model-based diagnostics** | **Limiting cell properties**

D. Witt, L. Bläubaum, F. Baakes, U. Krewer*

1 – 14

Origin of Performance Improvements in Lithium-Ion Cells after Fast Formation

Impact of fast formation on cell performance. This study combines an experimental formation study with a model-based cell diagnosis. The experiments highlight that the formation procedure can profoundly influence the fast charge/discharge capacity. The model-based analysis indicates that changes in effective transport properties in anode and cathode drive these performance differences.